Journal of the Optical Society of America B
OPTICAL PHYSICS

Metatronic analogues of the Wheatstone bridge

YUE LI,[1,2] IÑIGO LIBERAL,[2] AND NADER ENGHETA[2,*]

[1]Department of Electrical Engineering, Tsinghua University, Beijing 100084, China
[2]Department of Electrical and Systems Engineering, University of Pennsylvania, Philadelphia, Pennsylvania 19104, USA
*Corresponding author: engheta@ee.upenn.edu

Received 5 October 2015; revised 21 December 2015; accepted 21 December 2015; posted 24 December 2015 (Doc. ID 251366); published 1 February 2016

The Wheatstone bridge is a classical electrical circuit developed by Sir Charles Wheatstone in the middle of the 19th century. The operating principle of the Wheatstone bridge is based on the concept of a difference measurement, and it is one of the most popular circuits in the characterization of resistors. Here, we utilize the optical metatronic paradigm—metamaterial-inspired optical nanocircuitry—to extend the use of the Wheatstone bridge to different platforms and frequency regimes. Specifically, using numerical simulations we present three different designs in which the analogue of the Wheatstone bridge concept is implemented on all-optical metamaterial boards, microwave waveguides, and planar silicon photonic systems, operating in frequency bands ranging from microwaves to the visible. The proposed devices enrich the collection of available nanocircuitry, and it is shown that high accuracy and simplicity of the Wheatstone bridge can be transplanted and exploited in multiple nanophotonic applications including, e.g., the characterization of nanoparticles.

OCIS codes: (160.3918) Metamaterials; (160.0160) Materials; (160.4760) Optical properties; (160.1245) Artificially engineered materials; (250.5300) Photonic integrated circuits; (350.4238) Nanophotonics and photonic crystals.

http://dx.doi.org/10.1364/JOSAB.33.000A72

1. INTRODUCTION

The Wheatstone bridge is a popular electrical circuit commonly used to determine the value of unknown resistors based on the concept of a difference measurement. The circuit was first proposed by Samuel Hunter Christie [1], but it is named after Sir Charles Wheatstone, who developed and popularized it in the mid-19th century [2,3]. In fact, the clear and elegant analysis carried out by Wheatstone represented one of the first practical applications of Ohm's law [3]. As schematically depicted in Fig. 1(a), the classical Wheatstone bridge is driven by a battery, and it is composed of an ammeter and four resistors, including two known resistors (R1 and R2), a variable resistor (R3), and an unknown resistor (R4). Its principle of operation is strikingly simple: when the ratios between the resistors R1/R2 and R3/R4 are balanced, then there is no current flowing through the ammeter. In this manner, by adjusting the value of R3 to obtain the minimum current on the ammeter, the value of R4 can be determined with a simple formula: $R4 = R2 \cdot R3/R1$. Aside from historical reasons, the popularity of the Wheatstone bridge is justified by the main advantages of its null method, including its high accuracy, inherent simplicity, and ease of fabrication.

Naturally, the Wheatstone bridge has evolved since the 19th century, and it is now utilized as a versatile measurement tool that, aside from resistors, also enables the characterization of other impedance elements, such as inductors and capacitors, as well as those physical quantities that have an impact over the impedance of a lumped element (e.g., force, temperature, pressure, soil composition, and the amount of combustible gases in a sample). Furthermore, the Wheatstone bridge and other balanced sensing configurations have also been utilized in integrated optics systems [4] and optical fiber [5]. Recently, implementations of Wheatstone bridges at the nanoscale have opened up the exciting possibility of sensing, detecting, and recognizing a single molecule [6–8]. In these works, symmetrical nanoparticles and nanowires are built to mimic the function of a Wheatstone bridge, and the accuracy of the measurement benefits from the same operating principle as the original electrical circuit.

Here, we propose to extend the use of the Wheatstone bridge to the field of optical metatronics, i.e., metamaterial-inspired optical nanocircuitry [9,10]. This nanocircuit paradigm merges the fields of electronics and photonics, enabling the design of optical nanocircuits as the combination of "lumped" elements [9,10], such as nanoinductors and nanocapacitors, which are connected via reactive coupling, waveguide devices, and/or D-dot wires [11–13]. Successful examples of the application of optical metatronic concepts include the matching [14–16] and design [17] of nanoantennas, optical nanofilters [18–20], wireless optical links [21,22], as well as the modular assembly of nanoparticle clusters [23]. In essence, metatronics makes it possible to take advantage of both the vast knowledge and the tools of circuit theory,

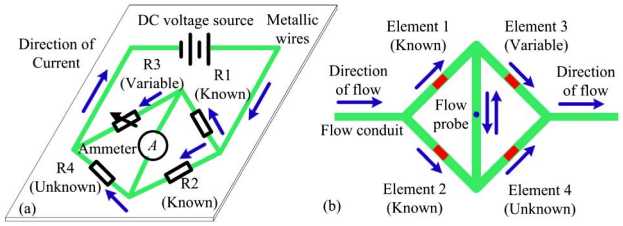

Fig. 1. Conceptual sketch of the generalized Wheatstone bridge. (a) Sketch of the classical Wheatstone bridge. (b) Generalized Wheatstone bridge for any generic physical entity flowing in the conduits with four arms and a bridge connecting the two sections. Analogous to the concept of Wheatstone bridge, the proper balance among the four elements in the path of this flow provides a technique for metrology of unknown elements.

translating them into optics. Inspired by this approach, this work particularly aims at the implementation of optical metatronic analogues of the classical Wheatstone bridge. We emphasize that many nanophotonic systems could benefit from the high accuracy and simplicity of the Wheatstone bridge, enabling, for example, the characterization of the intrinsic properties of nanoparticles. Characterization devices based on this principle could mitigate the difficulties imposed by the nontrivial and size-dependent properties of the nanoparticles permittivity (see, e.g., [24]).

To this end, we present three different examples in which the Wheatstone bridge is implemented over three different physical platforms and operating in three different frequency regimes. These examples include an implementation that is a direct translation of the classical circuit in optical metatronic terms. However, we also demonstrate that, due to fundamental symmetry configurations, the use of the Wheatstone circuit can be extended beyond the realm of circuit theory, i.e., it can be applied in devices where the response of the systems is not determined by Kirchoff's laws. This concept is illustrated in Fig. 1(b), which represents a generalized version of the Wheatstone bridge, aimed to control the flow of a certain physical entity. The structure of the generalized system is composed of a certain type of conduit (shown in green) that guides the path of flow of a generic physical entity (shown as blue arrows). In addition, the flow of this entity is influenced by four elements (shown in red) immersed within the conduits. As is the original Wheatstone bridge, two of them are known, one is tunable, and there is an unknown element. In this generalized case, the operation of the system can be then justified based on fundamental symmetry properties. In essence, if the two known elements are identical then it is clear that the structure is perfectly symmetrical. Therefore, the flow of any generic physical entity cannot have a preferred direction on the middle arm, and hence it must be zero, justifying the use of a null method.

2. RESULTS AND DISCUSSION

A. Metatronic Wheatstone Bridge at Optical Frequencies

Our first design consists of a two-dimensional (2D) optical metatronic circuit formed on an all-optical metamaterial circuit board [11]. We emphasize that in this first example the optical metatronic circuit obeys the same Kirchhoff's current and voltage laws as in conventional electrical circuits [9]; hence, the classical Wheatstone bridge can be directly translated to the alphabets of these metamaterial-inspired nanocircuits. As schematically depicted in Fig. 2(a), the current flowing in this metatronic circuit is the displacement current [9,10], $-i\omega\boldsymbol{D}$, whose flow is controlled by using D-dot wires [11–13], i.e., air grooves carved out in the background epsilon-near-zero (ENZ) medium composing the nanocircuit board. In our numerical simulation of this structure, the circuit is driven by an electric current dipole moment of 1 A·m oriented along $\hat{\mathbf{x}}$ and oscillating at 750 THz ($\lambda_0 = 400$ nm), and the displacement currents excited by the dipole are numerically obtained in the middle of the center channel. We use the RF module of the finite element method software COMSOL Multiphysics 4.3b. Triangular meshing is built with a maximum element size of $\lambda_0/40$, where λ_0 is the free-space wavelength. The choice of this frequency in our simulation is arbitrary, and a different range of frequencies can be readily considered.

The four impedances of the bridge are implemented with "lumped" nanoparticles with different relative permittivities ε_1, ε_2, ε_3, and ε_4. Once again, the unknown value of ε_4 can be determined by tuning ε_3 until the displacement current $-i\omega D_y$ in the middle channel is minimized. In practice, the variable element with tunable permittivity ε_3 could be controlled, for example, by using liquid crystals (see, e.g., [25–28]) or phase-transition materials (see, e.g., [29–32]). The permittivity of these materials could be adjusted by changing the temperature of the element or applying a bias voltage. Without loss of generality, in our simulation we consider a bridge loaded with four optical nanoinductors formed by plasmonic nanoparticles with negative relative permittivity: $\varepsilon_1 = \varepsilon_2 = -2$ (known), $\varepsilon_4 = -4$ ("unknown"), and ε_3 variable. In principle, the choice of the first two elements is arbitrary, though its value can be optimized to improve the performance of the systems (e.g., sensitivity).

The performance of the proposed 2D configuration has been assessed with COMSOL MultiPhysics 4.3b. In particular, Figs. 2(b) and 2(c) depict the magnitude and phase, respectively, of the $\hat{\boldsymbol{y}}$ component of the electric displacement field, D_y, obtained at the simulation probe as a function of the variable relative permittivity ε_3. As expected, the magnitude of D_y (proportional to the displacement current) is nearly zero at the balanced point $\varepsilon_3 = \varepsilon_4 = -4$. Moreover, the phase of D_y undergoes a 180 deg phase variation around that point, evidencing a change in the direction of the current flow. The effect of loss on the performance of the system is also investigated in Figs. 2(b) and 2(c), which include the magnitude and phase of D_y at the probe location as a function of the imaginary part of relative permittivity of the ENZ background. It can be concluded from Figs. 2(b) and 2(c) that the principle of operation of the system is not, in principle, affected by losses. This is evidenced by the fact that, independent of the amount of loss, all curves represented in Fig. 2(b) preserve a zero crossing when the permittivity of the variable element equals the permittivity of the "unknown" element. In essence, losses decrease the magnitude of the fields on each of the arms of the Wheatstone bridge, but this effect does not affect the "equilibrium" conditions in which the sensing mechanism is based. Therefore, the main detrimental impact of losses in the proposed systems is a

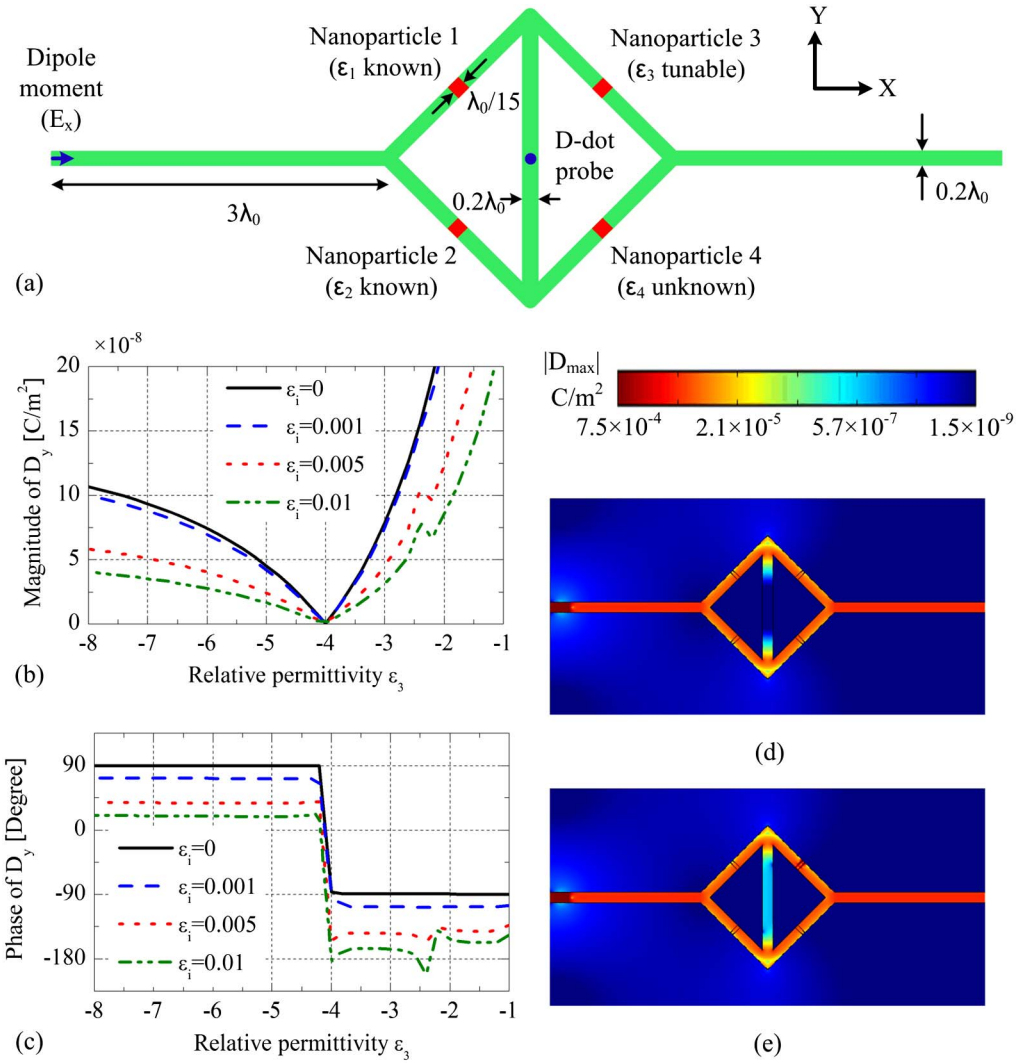

Fig. 2. Metatronic Wheatstone bridge at optical frequencies. (a) Sketch and dimensions of the 2D optical metatronic Wheatstone bridge operating at $\lambda_0 = 400$ nm (750 THz) formed by air grooves ("D-dot wire") carved in an epsilon-near-zero host, characterized by background relative permittivity $\varepsilon_r = 10^{-5}$. The circuit is driven by an electric current dipole moment of 1 A m, and the four nanoparticles are composed of nonmagnetic materials with relative permittivity shown below. (b) Magnitude and (c) phase of the $\hat{\boldsymbol{y}}$ component of the electric displacement field, D_y, obtained by the simulation probe in our numerical study for different amounts of loss, modeled as the imaginary part of the relative permittivity of the background ENZ medium, as a function of the tunable relative permittivity ε_3; for $\varepsilon_1 = \varepsilon_2 = -2$ and $\varepsilon_4 = -4$. (d), (e) Simulation results for the distribution of the magnitude of the electric displacement field for both (d) the lossless balanced case with $\varepsilon_1 = \varepsilon_2 = -2$ and $\varepsilon_3 = \varepsilon_4 = -4$, and (e) a lossless unbalanced configuration with $\varepsilon_1 = \varepsilon_2 = -2$, $\varepsilon_3 = -1$, and $\varepsilon_4 = -4$. Note the logarithmic color scale bar.

reduction of the sensitivity, which appears as a reduction in the slope of the curves at their zero crossing.

In order to illustrate further the performance of the metatronic Wheatstone bridge, Figs. 2(d) and 2(e) show the distribution of the magnitude of electric displacement field in the 2D circuit for both the balanced case [Fig. 2(d), $\varepsilon_1 = \varepsilon_2 = -2$ and $\varepsilon_3 = \varepsilon_4 = -4$] and one of the unbalanced configurations [Fig. 2(e), $\varepsilon_1 = \varepsilon_2 = -2$, $\varepsilon_3 = -1$, and $\varepsilon_4 = -4$] with a lossless background ENZ medium. It is evident from this figure that the current is nearly zero in the balanced case, by contrast with the significant current flowing though the central arm in the unbalanced case. Therefore, it can be concluded that the response of the metatronic Wheatstone bridge follows exactly the same operating principle as the classical Wheatstone bridge, thus opening up the possibility of characterizing nanoparticles within a nanocircuit metasurface.

B. Metallic Waveguide Wheatstone Bridge Operating at Microwave Frequencies

As was anticipated, symmetry considerations reveal that the principle of operation of the Wheatstone bridge can be translated to a wider class of systems beyond the realm of electrical circuits. This second example studies the implementation of a Wheatstone bridge where the electromagnetic energy flow (i.e., the time-averaged Poynting vector field) plays the role of electrical current, whereas the wires or conduits are assumed to be waveguides. For the sake of simplicity, we consider first a 2D waveguide bounded by perfect electric conductor (PEC)

walls and filled with air [see Fig. 3(a)]. This waveguide supports transverse electromagnetic (TEM) model [33,34], and in our simulation using the RF module of COMSOL Multiphysics 4.3b, the incident wave at the input wave port with an incident TEM mode with power of 1 W is assumed to be polarized with H_z and E_y components. Without loss of generality, the frequency of operation of this proof-of-concept design is fixed at 300 MHz. Furthermore, the bridge is loaded with four subwavelength dielectric slabs with relative permittivity $\varepsilon_1 = \varepsilon_2 = 2$ (known), $\varepsilon_4 = 4$ ("unknown"), and ε_3 variable, that locally play the role of capacitors.

The value of the relative permittivity of the unknown dielectric slab (ε_4) is determined by adjusting the relative permittivity of tunable dielectric slab (ε_3) so that the power flow on the central waveguide is zero. In order to illustrate this fact, Fig. 3(b) depicts the $\hat{\boldsymbol{y}}$ component of the time-averaged Poynting vector field (power flow), S_y, which is assumed to be obtained in the middle of the central channel [see Fig. 3(a)]. It is apparent from Fig. 3(b) that S_y decreases as ε_3 increases with $S_y > 0$ for $\varepsilon_3 < 4$ and $S_y < 0$ for $\varepsilon_3 > 4$. That is to say, the power flow recorded by the simulation probe crosses zero at the balanced configuration. Figure 3(b) also depicts the y component of the time-averaged Poynting vector at the simulation probe position for different amounts of loss modeled as a finite conductivity of the waveguide walls. Similar to the previous example, the loss does not affect the principle of operation of the system, it simply results in a reduction of the in the slope of the curves at their zero crossing.

The operating principle of the metallic waveguide Wheatstone bridge can be more clearly appreciated by comparing the power flow in the balanced case [$\varepsilon_1 = \varepsilon_2 = 2$, $\varepsilon_3 = \varepsilon_4 = 4$, Fig. 3(c)] and in an unbalanced configuration [e.g., $\varepsilon_1 = \varepsilon_2 = 2$ $\varepsilon_3 = 2$, $\varepsilon_4 = 4$, Fig. 3(d)] inside the PEC waveguide. It is clear from those figures that the flow of power in the central arm vanishes for the balanced case, whereas in the unbalanced case there is a significant flow of power going from the lower to the upper arms. For the sake of completeness, the electric and magnetic field distributions in the device are reported in Figs. 4(a) and 4(b), which reveal very distinct electric and magnetic field distributions in the top and bottom arms of the waveguide. Furthermore, although the field in the central arm is dominated by a standing wave in both balanced and unbalanced cases, the difference between both configurations can be clearly appreciated in Fig. 4(c), which depicts the magnitude of the magnetic field along the central waveguide channel. It is apparent from Fig. 4(c) that both configurations exhibit different field distributions. On one hand, the balanced case is characterized by the excitation of an almost pure standing wave, featuring well-defined zeros of the magnetic field (and thus an almost zero net time-averaged Poynting vector). On the

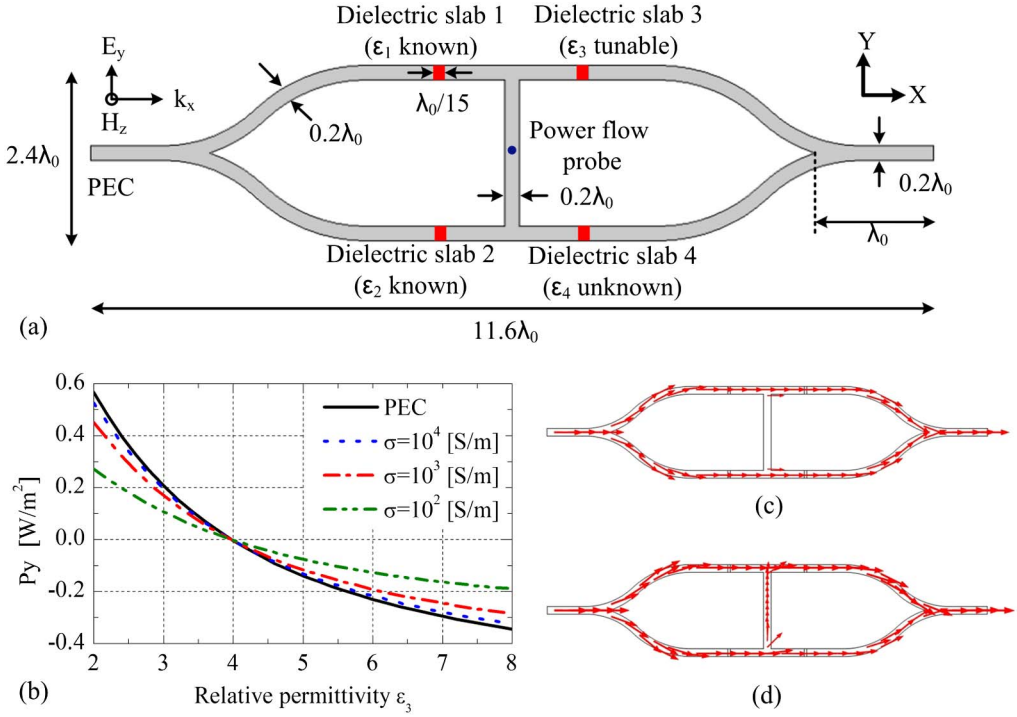

Fig. 3. Two-dimensional parallel-plate metallic waveguide Wheatstone bridge operating at microwave frequencies. (a) Sketch and dimensions of a waveguide-based Wheatstone bridge operating at $\lambda_0 = 1$ m (300 MHz). In our simulation, the waveguide is filled with air and bounded by PEC walls. The waveguide is excited with an incident TEM mode with power of 1 W. The four dielectric slabs have relative permittivity values shown below. (b) $\hat{\boldsymbol{y}}$ component of the time-averaged Poynting vector field (power flow), obtained at the simulation probe as a function of the tunable relative permittivity ε_3; for $\varepsilon_1 = \varepsilon_2 = 2$ and $\varepsilon_4 = 4$, and for different conductivities of the metallic waveguide walls. (c), (d) Simulation results for the distribution of the Poynting vector field in a PEC waveguide for both (c) the balanced case with $\varepsilon_1 = \varepsilon_2 = 2$ and $\varepsilon_3 = \varepsilon_4 = 4$, and (d) an unbalanced configuration with $\varepsilon_1 = \varepsilon_2 = 2$, $\varepsilon_3 = 2$, and $\varepsilon_4 = 4$. The magnitude of the power flow is described by the size of the arrows following a logarithmic scale.

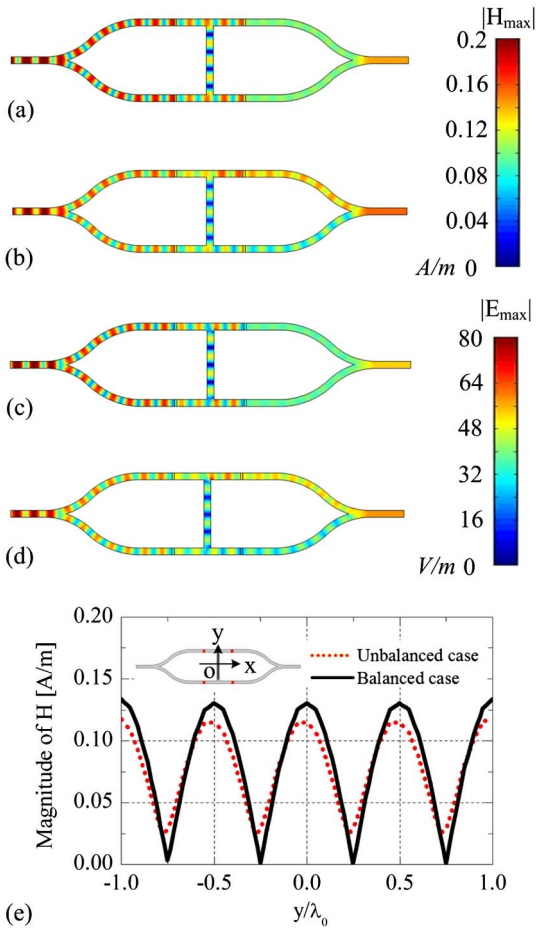

Fig. 4. Magnitudes of the (a), (b) magnetic and (c), (d) electric field distributions inside the PEC waveguide shown in Fig. 3(a) operating at 300 MHz. (a), (c) balanced case with $\varepsilon_1 = \varepsilon_2 = 2$ and $\varepsilon_3 = \varepsilon_4 = 4$, and (b), (d) unbalanced case with $\varepsilon_1 = \varepsilon_2 = 2$, $\varepsilon_3 = 2$, and $\varepsilon_4 = 4$. (e) Magnetic field magnitude distribution along the central channel for both balanced and unbalanced cases.

other hand, the minima observed in the unbalanced case never reach zero, which is an unequivocal sign of a partial standing wave and the propagation of nonzero time-averaged power along the waveguide. This behavior can be quantitatively assessed by computing the voltage standing wave ratio (VSWR) associated with these field distributions. In particular, the field distributions depicted in Fig. 4(c) of the balanced and unbalanced cases result is VSWR values of 510.3 and 4.6, respectively, which evidence a transition from pure standing-wave to partial standing-wave propagation phenomena.

C. Silicon Photonics Wheatstone Bridge Metasurface Operating at the Near-Infrared

In practice, the generic design introduced in the previous section can be extrapolated to virtually any waveguide system. Arguably, the most natural transition from a 2D waveguide model to an actual 3D device might be based on a rectangular metallic waveguide supporting a TE_{10} mode [33,34]. However, this design is left for future efforts, and here we analyze yet another alternative based on silicon (Si) photonics operating at $\lambda_0 = 1550$ nm. This choice is motivated due to the great interest of this planar technology in the development of optical communication components [35–37]. The geometry and dimensions of the proposed device are sketched in Fig. 5(a), and a full 3D model is included in Fig. 5(b). In this case, the planar system is formed by using Si waveguides, and the middle channel of the bridge is replaced by a microring resonator (see the Acknowledgment section). On one hand, the waveguides are designed to support a TM_{10} incident mode with H_z, E_x, and E_y components at the wavelength of operation $\lambda_0 = 1550$ nm. On the other hand, the choice of the planar microring resonator is motivated as it provides a strong coupling between the top and bottom waveguides, as well as for its popularity as one of the main components of silicon photonics [38–40]. We emphasize that the microring can couple the energy simultaneously from both the upper and lower Si waveguides. Thus, if the fields couple from both sides with identical magnitude and phase, the power flow inside the microring is very small and nearly "static," i.e., the fields inside the microring form a standing wave. By contrast, if the fields that are coupled from both sides are different, a large power flow rotates inside the microring, and a partial standing wave is formed. To prove this fact, we also include four dielectric slabs (shown in yellow) characterized by relative permittivity: $\varepsilon_1 = 2$ (unknown), ε_2 (tunable), and $\varepsilon_3 = \varepsilon_4 = 4$ (known). In this case, the dielectric slabs/capacitors corresponding to the unknown (ε_1) and tunable (ε_2) impedances are arranged ahead of the microring, since it was found that this configuration provided an enhanced difference of power flow inside the microring. Similar to previous designs, a simulation probe is positioned in the microring in order to record the electromagnetic power flow (time-averaged Poynting vector field) in our numerical simulation.

The performance of the device was investigated numerically using the software package CST Microwave Studio. The time domain solver is adopted with automatic tetrahedral meshing. The source is a waveguide port with the incident mode carrying power of 1 W. Figure 5(c) depicts the $\hat{\boldsymbol{y}}$ component of the time-averaged power flow, S_y, recorded by the probe, as a function of the tunable permittivity (ε_2) for different amounts of loss of the waveguide material as parameterized by the loss tangent. Note that due to the location of the probe, a clockwise (counterclockwise) rotation is associated with a negative (positive) value of S_y. In this manner, it is apparent from Fig. 5(c) that the power flow rotates clockwise (counterclockwise) for $\varepsilon_2 < 2$ ($\varepsilon_2 > 2$). Moreover, the power flow is nearly zero at the balanced case $\varepsilon_2 = 2$, which enables the characterization of dielectrics by using the null method. The simulation results for the distribution of the power flow inside the device without loss are depicted in Figs. 5(d) and 5(e), for both the balanced case [Fig. 5(d), $\varepsilon_1 = \varepsilon_2 = 2$ and $\varepsilon_3 = \varepsilon_4 = 4$] and an unbalanced configuration [Fig. 5(e), $\varepsilon_1 = 2$, $\varepsilon_2 = 8$, and $\varepsilon_3 = \varepsilon_4 = 4$]. These figures ratify that the power flow is small and symmetric in the balanced case, while it is large and rotating counterclockwise in the unbalanced configuration with $\varepsilon_2 > 2$. Additional insight on the dynamics of the device can be obtained by inspecting the electric and magnetic field distributions, which are shown in Fig. 6, for both balanced and unbalanced cases.

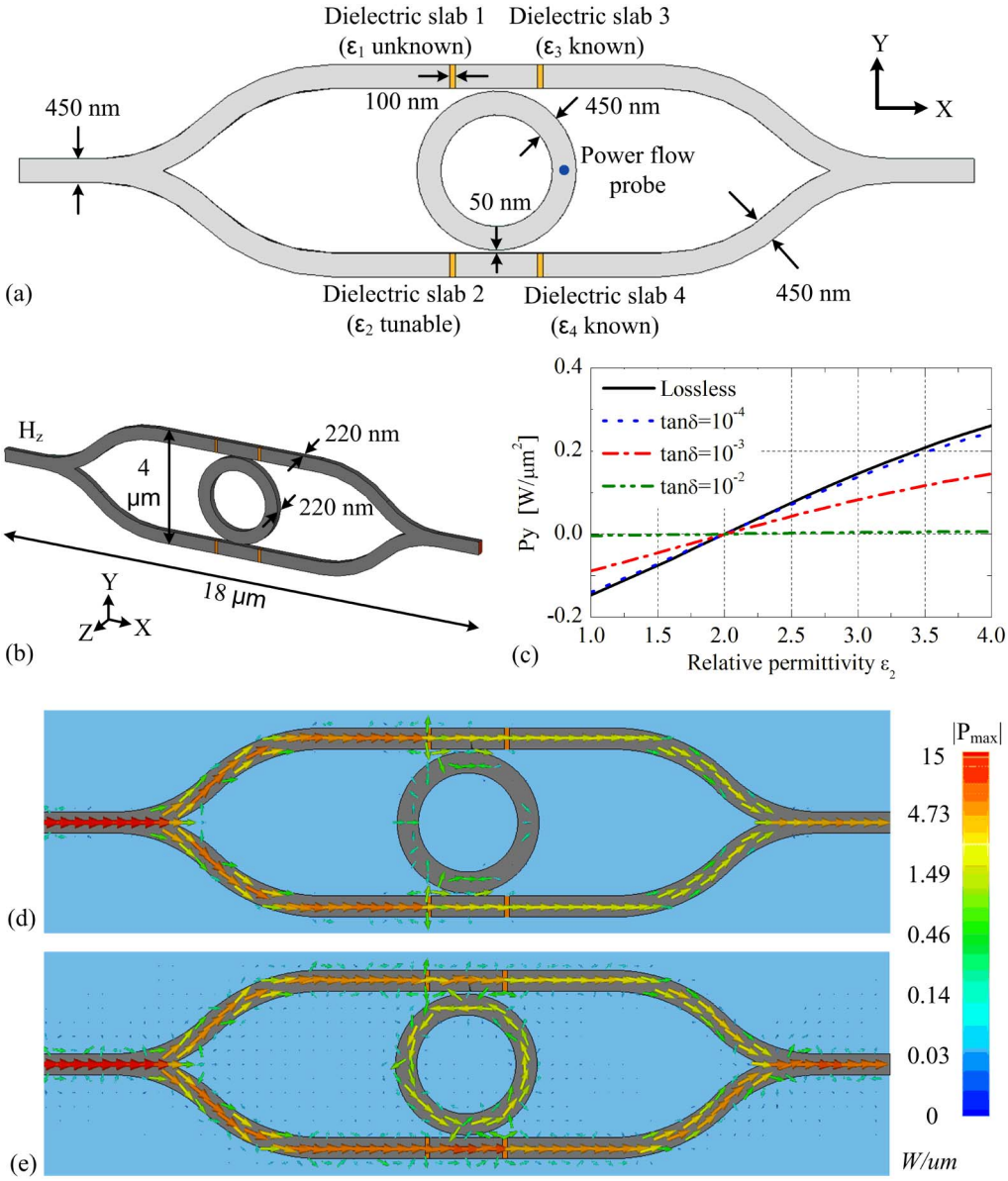

Fig. 5. Silicon photonics Wheatstone bridge metasurface operating at the near-infrared (NIR). (a) Sketch and dimensions of a Si photonics-based Wheatstone bridge, composed of Si waveguides and a microring resonator operating at $\lambda_0 = 1550$ nm. (b) Three-dimensional view of the simulation setup. The system is excited through a waveguide port with the incident mode carrying power of 1 W. The four nanoslabs are of nonmagnetic materials with relative permittivity shown below. (c) $\hat{\boldsymbol{y}}$ component of the time-averaged Poynting vector field (power flow) with different loss tangents (tan δ) of the Si waveguide material, as a function of the tunable relative permittivity ε_2, for $\varepsilon_3 = \varepsilon_4 = 4$ and $\varepsilon_1 = 2$. (d), (e) Simulation results of the distribution of the power flow inside the proposed device (tan $\delta = 0$) for both (d) the balanced case with $\varepsilon_1 = \varepsilon_2 = 2$ and $\varepsilon_3 = \varepsilon_4 = 4$ and (e) an unbalanced configuration with $\varepsilon_1 = 2$, $\varepsilon_2 = 8$, and $\varepsilon_3 = \varepsilon_4 = 4$. Note the logarithmic color scale bar. We can clearly see the proper operation of this device as a Si photonics Wheatstone bridge.

Finally, it is worth mentioning that the sensitivity of system depends on the values of the two known elements, as shown in Fig. 7. It can be seen from this figure that the system would perform a correct prediction of the permittivity value of the "unknown" element independently of the values of two "known" elements, i.e., all curves exhibit a zero crossing when the permittivity of the variable element equals the permittivity of the "unknown" element. However, it is also clear from Fig. 7 that the sensitivity of the system, understood as the slope of the curve at the zero crossing, is a function of the permittivity of the two known elements. In particular, the sensitivities of the metallic waveguide Wheatstone bridge [Fig. 7(c)] and the silicon photonics Wheatstone bridge [Fig. 7(d)] are maximized for permittivity values of approximately $\varepsilon_1 = \varepsilon_2 = 2$ and $\varepsilon_3 = \varepsilon_4 = 4$, respectively, which are actually the values employed in the examples presented in Figs. 3 and 5. By contrast, Figs. 7(a) and 7(b) reveal that the sensitivity of the metatronic Wheatstone bridge is almost independent of the values of $\varepsilon_1 = \varepsilon_2$. This is

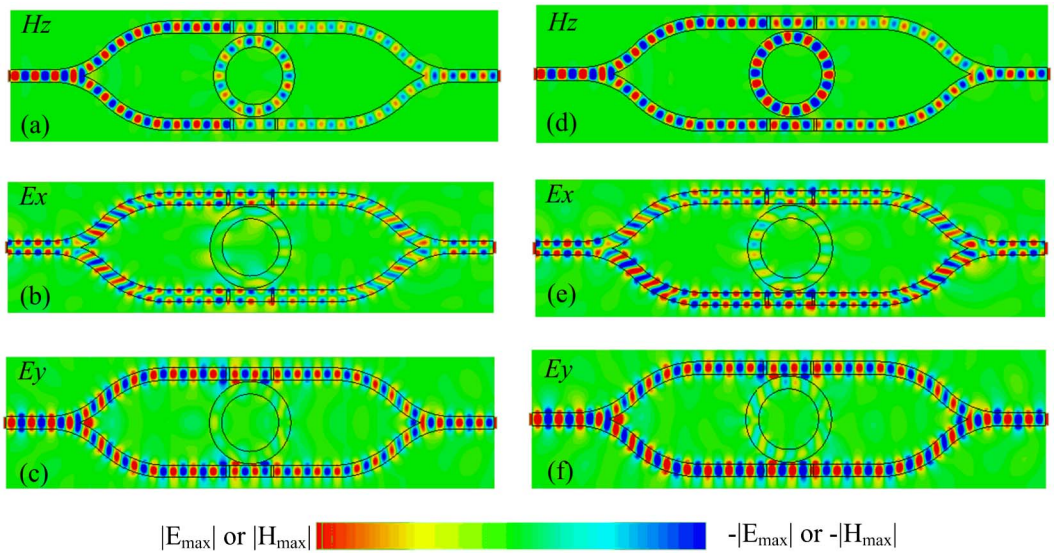

Fig. 6. Snapshots of the (a), (d) H_z, (b), (e) E_x, and (c), (f) E_y field component distributions inside the Si waveguide depicted in Fig. 5(a) operating at 193.5 THz ($\lambda = 1550$ nm) for both (a), (c) the balanced case with $\varepsilon_1 = \varepsilon_2 = 2$ and $\varepsilon_3 = \varepsilon_4 = 4$ and (d), (f) an unbalanced configuration with $\varepsilon_1 = 2$, $\varepsilon_2 = 8$, and $\varepsilon_3 = \varepsilon_4 = 4$.

due to the fact that the displacement current is mostly determined by the impedance of the D-dot wire, and changes in the impedances of the first and second elements have lesser influence.

3. CONCLUSIONS

In conclusion, by using metatronic concepts and fundamental symmetry considerations, we demonstrate that it is possible to translate the Wheatstone bridge electrical circuit to different

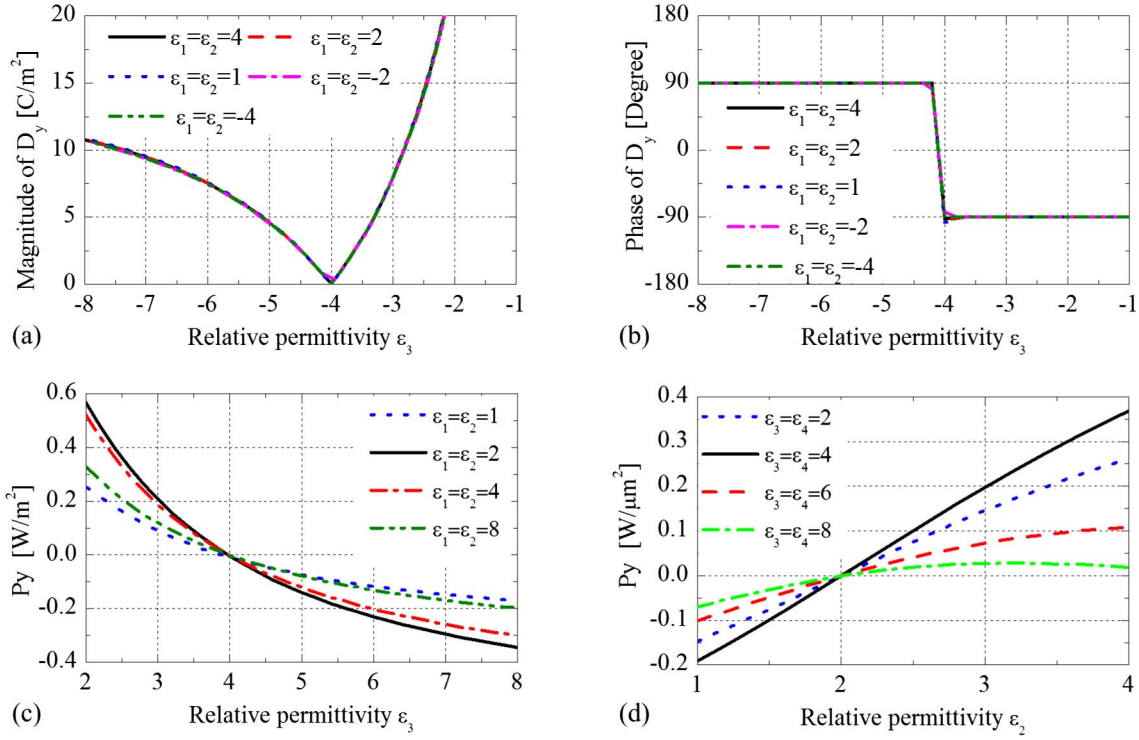

Fig. 7. Sensitivity variation. (a) Magnitude and (b) phase of y component of electric displacement field D_y at the probe position of metatronic Wheatstone bridge, for different permittivity values of the "known" elements $\varepsilon_1 = \varepsilon_2$. The system corresponds to the setup studied in Fig. 2. (c), (d) y component of the time-averaged Poynting vectors at the probe positions of the metallic waveguide Wheatstone bridge and of the silicon photonics Wheatstone bridge, respectively, for different permittivity values of the "known" elements. The systems shown in (c) and (d) correspond to the setups studied in Figs. 3 and 5, respectively.

platforms (all-optical metamaterial circuit boards, microwave waveguides, and planar silicon photonics) and different frequency regimes (microwaves, NIR, and visible). These new devices enrich the collection of optical nanocircuitry elements and, in this manner, optical nanocircuits can benefit from the high accuracy and inherent simplicity of the classical Wheatstone bridge, with important metrology applications including, for example, the characterization of nanoparticles.

Funding. Office of Naval Research (ONR) (N00014-10-1-0942); Air Force Office of Scientific Research (AFOSR) (FA9550-14-1-0389); National Natural Science Foundation of China (NSFC) (61301001).

Acknowledgment. Y. Li was partially supported by the National Natural Science Foundation of China (NSFC) under grant 61301001. N. E. is grateful to Professor Anatoly Zayats and the Physics Department of the King's College London for their invitation to deliver the 2015 Wheatstone Lecture, which initiated this research. The authors are also thankful to Professor Niek van Hulst of ICFO, Spain, for insightful questions and his suggestion about the use of microrings during the question and answer session immediately following this Wheatstone Lecture.

REFERENCES

1. S. H. Christie, "The Bakerian Lecture: experimental determination of the laws of magneto-electric induction in different masses of the same metal, and of its intensity in different metals," Philos. Trans. R. Soc. London **123**, 95–142 (1833).
2. C. Wheatstone, "The Bakerian Lecture: an account of several new instruments and processes for determining the constants of a voltaic circuit," Philos. Trans. R. Soc. London **133**, 303–327 (1843).
3. S. Ekelof, "The genesis of the Wheatstone bridge," Eng. Sci. Educ. J. **10**, 37–40 (2001).
4. M. McCourt, F. Corning, and F. Avon, "Passive integrated optics for optical communications," in *Integrated Optics* (Information Gatekeepers, 1994), Vol. **13**.
5. B. E. Jones, "Optical fibre sensors and systems for industry," J. Phys. E. **18**, 770–782 (1985).
6. S. Ami, M. Hliwa, and C. Joachim, "Balancing a four-branch single-molecule nanoscale Wheatstone bridge," Nanotechnology **14**, 283–289 (2003).
7. T. J. Davis, K. C. Vernon, and D. E. Gómez, "A plasmonic 'ac Wheatstone bridge' circuit for high-sensitivity phase measurement and single-molecule detection," J. Appl. Phys. **106**, 043502 (2009).
8. C. Maedler, S. Erramilli, L. J. House, M. K. Hong, and P. Mohanty, "Tunable nanowire Wheatstone bridge for improved sensitivity in molecular recognition," Appl. Phys. Lett. **102**, 043112 (2013).
9. N. Engheta, A. Salandrino, and A. Alù, "Circuit elements at optical frequencies: nanoinductors, nanocapacitors, and nanoresistors," Phys. Rev. Lett. **95**, 095504 (2005).
10. N. Engheta, "Circuits with light at nanoscales: optical nanocircuits," Science **317**, 1698–1702 (2007).
11. A. Alù and N. Engheta, "All optical metamaterial circuit board at the nanoscale," Phys. Rev. Lett. **103**, 143902 (2009).
12. M. G. Silveirinha, A. Alù, J. Li, and N. Engheta, "Nanoinsulators and nanoconnectors for optical nanocircuits," J. Appl. Phys. **103**, 064305 (2008).
13. B. Edwards and N. Engheta, "Experimental verification of displacement-current conduits in metamaterials-inspired optical circuitry," Phys. Rev. Lett. **108**, 193902 (2012).
14. A. Alù and N. Engheta, "Input impedance, nanocircuit loading, and radiation tuning of optical nanoantennas," Phys. Rev. Lett. **101**, 043901 (2008).
15. A. Alù and N. Engheta, "Tuning the scattering response of optical nanoantennas with nanocircuit loads," Nat. Photonics **2**, 307–310 (2008).
16. N. Liu, F. Wen, Y. Zhao, Y. Wang, P. Nordlander, N. J. Halas, and A. Alù, "Individual nanoantennas loaded with three-dimensional optical nanocircuits," Nano Lett. **13**, 142–147 (2013).
17. J. Li, A. Salandrino, and N. Engheta, "Shaping light beams in the nanometer scale: a Yagi-Uda nanoantenna in the optical domain," Phys. Rev. B **76**, 245403 (2007).
18. A. Alù, M. E. Young, and N. Engheta, "Design of nanofilters for optical nanocircuits," Phys. Rev. B **77**, 144107 (2008).
19. Y. Sun, B. Edwards, A. Alù, and N. Engheta, "Experimental realization of optical lumped nanocircuits at infrared wavelengths," Nat. Mater. **11**, 208–212 (2012).
20. H. Caglayan, S.-H. Hong, B. Edwards, C. R. Kagan, and N. Engheta, "Near-infrared metatronic nanocircuits by design," Phys. Rev. Lett. **111**, 073904 (2013).
21. A. Alù and N. Engheta, "Wireless at the nanoscale: optical interconnects using matched nanoantennas," Phys. Rev. Lett. **104**, 213902 (2010).
22. D. Dregely, K. Lindfors, M. Lippitz, N. Engheta, M. Totzeck, and H. Giessen, "Imaging and steering an optical wireless nanoantenna link," Nat. Commun. **5**, 4354 (2014).
23. J. Shi, F. Monticone, S. Elias, Y. Wu, D. Ratchford, X. Li, and A. Alù, "Modular assembly of optical nanocircuits," Nat. Commun. **5**, 3896 (2014).
24. U. Kreibig and M. Vollmer, *Optical Properties of Metal Clusters* (Springer, 1995).
25. A. Drozd-Rzoska, S. J. Rzoska, and J. Zioło, "Critical behavior of dielectric permittivity in the isotropic phase of nematogens," Phys. Rev. E **54**, 6452–6456 (1996).
26. S. J. Rzoska, J. Ziolo, W. Sułkowski, J. Jadżyn, and G. Czechowski, "Fluidlike behavior of dielectric permittivity in a wide range of temperature above and below the nematic-isotropic transition," Phys. Rev. E **64**, 052701 (2001).
27. F. Yang and J. R. Sambles, "Determination of the microwave permittivities of nematic liquid crystals using a single-metallic slit technique," Appl. Phys. Lett. **81**, 2047–2049 (2002).
28. H.-C. Lin and Y.-H. Lin, "An electrically tunable-focusing liquid crystal lens with a low voltage and simple electrodes," Opt. Express **20**, 2045–2052 (2012).
29. H. S. Choi, J. S. Ahn, J. H. Jung, T. W. Noh, and D. H. Kim, "Mid-infrared properties of a VO_2 film near the metal-insulator transition," Phys. Rev. B **54**, 4621–4628 (1996).
30. B.-G. Kim, S. M. Cho, T.-Y. Kim, and H. M. Jang, "Giant dielectric permittivity observed in Pb-based perovskite ferroelectrics," Phys. Rev. Lett. **86**, 3404–3406 (2001).
31. J. Wu, C.-W. Nan, Y. Lin, and Y. Deng, "Giant dielectric permittivity observed in Li and Ti doped NiO," Phys. Rev. Lett. **89**, 217601 (2002).
32. A. A. Bokov, Y.-H. Bing, W. Chen, Z.-G. Ye, S. A. Bogatina, I. P. Raevski, S. I. Raevskaya, and E. V. Sahkar, "Empirical scaling of the dielectric permittivity peak in relaxor ferroelectrics," Phys. Rev. B **68**, 052102 (2003).
33. C. Balanis, *Advanced Engineering Electromagnetics*, 2nd ed. (Wiley, 2012).
34. D. M. Pozar, *Microwave Engineering*, 4th ed. (Wiley, 2012).
35. G. T. Reed and A. P. Knights, *Silicon Photonics* (Wiley, 2004).
36. B. Jalali and S. Fathpour, "Silicon photonics," J. Lightwave Technol. **24**, 4600–4615 (2006).
37. M. Lipson, "Guiding, modulating, and emitting light on silicon-challenges and opportunities," J. Lightwave Technol. **23**, 4222–4238 (2005).
38. S. Xiao, M. H. Khan, H. Shen, and M. Qi, "Silicon-on-insulator microring add-drop filters with free spectral ranges over 30 nm," J. Lightwave Technol. **26**, 228–236 (2008).
39. A. M. Prabhu, A. Tsay, Z. Han, and V. Van, "Extreme miniaturization of silicon add-drop microring filters for VLSI photonics applications," IEEE Photon. J. **2**, 436–444 (2010).
40. S. B. Dey, S. Mandal, and N. N. Jana, "Quadruple optical ring resonator based filter on silicon-on-insulator," Optik **124**, 2920–2927 (2013).